Steady State Gas Flow from Tight Shale Matrix Subject to Water Blocking

Pål Østebø Andersen[1]

1 Department of Energy Resources, University of Stavanger, 4036 Norway

Abstract

This work studies 1D steady state flow of gas from compressible shale matrix subject to water blocking towards a neighbouring fracture. Water blocking is a capillary end-effect causing wetting phase (e.g. water) to accumulate near the transition from matrix to fracture. Hydraulic fracturing is essential for economical shale gas production. Water is frequently used as fracturing fluid, but its accumulation in the matrix can reduce gas mobility and production rate.

Gas transport is considered at a defined pressure drop. The model accounts for apparent permeability (slip), compressibility of gas and shale, permeability reduction, saturation tortuosity (reduced relative permeability upon compaction) and multiphase flow parameters like relative permeability and capillary pressure, which depend on wettability. The behavior of gas flow rate and distributions of gas saturation, pressure and permeability subject to different conditions and the stated mechanisms is explored.

Water blockage reduces gas relative permeability over a large zone and reduces gas flow rate. Despite gas flowing, strong capillary forces sustain mobile water over the entire system. Reducing drawdown gave lower driving force and higher resistance (by water blockage) for gas flow. 75 % reduction of drawdown made the gas flow rate a couple orders of magnitude lower compared to if there was no blockage. The impact was most severe in more water-wet systems.

The blockage caused most of the pressure drop to occur near the outlet. High pressure in the rest of the system reduced effects from gas decompression, matrix compression and slip-enhanced permeability while rapid gradients in all these effects occurred near the outlet. Gas decompression resulted in ~10 times higher Darcy velocity and pressure gradient near the outlet compared to inlet which contributed to removing blockage, but the added resistance reduced gas production rate. Similarly, higher gas Corey exponent associated gas flow with higher pressure drop. The result was less blockage, but lower gas production. Slip increased permeability, especially toward the outlet and contributed to increase gas production by 16 %.

Significant matrix compression was associated with permeability reduction and increased Corey exponent in some examples. These effects reduced production and shifted more of the pressure drop toward the outlet. Upstream pressure was more uniform and less compression and permeability reduction was seen overall compared to a system without water blockage.

Keywords: Water blocking; capillary end effects; shale gas production; compressible porous media

1. Introduction

1.1. Fracturing and water recovery

Gas shales have matrix permeability in nano- to microdarcy range (Javadpour et al. 2007; Mullen 2010). Economic production depends on multistage hydraulic fracturing with horizontal wells to generate a stimulated reservoir volume (SRV) (Yu and Sepehrnoori 2014). Large quantities of water are spent; Edwards and Celia (2018) reported 10 to 30 m^3 water per m horizontal well length for US shales. After fracturing, the well is opened for flowback of injected water (and gas production). It is then shut in for remaining water to soak some months before the well again is opened for production. Often, just a small fraction of the injected water returns. Singh (2016) mentions 6-10% as typical. The remaining water resides in the matrix or fractures. Residual saturations can permanently reduce gas mobility in these regions. Further, strong matrix capillary forces can lead to high trapped water saturations and low gas mobility near the matrix-fracture interface. This is refered to as water blockage (Holditch 1979). Besides affecting gas flow rates, the great water usage and loss is demanding on the environment. Water entrapment in the matrix and its effect on gas flow from matrix to fracture will be investigated in this work.

1.2. Water uptake

In addition to forced water invasion during fracturing, water uptake in shale can occur spontaneously (Xu and Deghanpour 2014; Makhanov et al. 2014; Yuan et al. 2014; Li et al. 2019). Capillary spontaneous imbibition, clay hydration and osmosis (salinity driven flow with shale as a semipermeable membrane) are suggested drive mechanisms (Xu and Deghanpour 2014; Singh 2016). Capillary forces increase as pore dimensions approach nanosize, and have great influence on fluid flow and trapping by driving wetting fluid to spread on the rock surface. Water droplets in air/gas have been reported to wet (spread on) shale surfaces in contact angle tests and can spontaneously imbibe and displace air in core samples (Borysenko et al. 2009; Xu and Deghanpour 2014; Lan et al. 2015; Wang et al. 2017; Luo et al. 2018). Capillary forces can explain this behavior due to the presence of hydrophilic matrix constituents. Shales consist of porous hydrophobic organic matter (kerogen), inorganic matter (clays and minerals) and microfractures (Sondergeld et al. 2010) and the latter two are often considered hydrophilic. Borysenko et al. (2009) however reported examples of both illite-rich hydrophilic shale and quartz- and kaolin-rich hydrophobic shale. Upon shale water uptake fluid-rock interactions can occur, including clay swelling, fines migration, mineral precipitation, induced micro-fractures, wettability alteration and water weakening (Holditch 1979; Chenevert and Pernot 1998; Ewy 2014; Yuan et al. 2014; Yan et al. 2015; Liu et al. 2016; Singh 2016; Li et al. 2019). Our focus will be on the capillary trapping of imbibed water near the fracture-matrix interface, which will be assumed to be a dominant mechanism.

1.3. Shale reservoir simulation

In simulation studies it is often assumed that hydraulic fractures are evenly spaced along a horizontal well, extend vertically to full formation height and symmetrically in opposite directions

of the well. One symmetrical unit is studied such as a fracture halflength and its surrounding matrix, or the SRV around a whole well. Hydraulic and natural fractures can be implemented explicitly, while the matrix is implemented with single porosity (Cipolla et al. 2010; Jurus et al. 2013; Beroncello et al. 2014; Ganjdanesh et al. 2016; Zhang et al. 2017; Wijaya and Sheng 2019; Berawala and Andersen 2020a,b; Elputranto and Akkutlu 2020) or multi-porosity (microfractures as a continuum connecting organic and inorganic pores) (Darishchev et al. 2013; Sun et al. 2015; Fakcharoenphol et al. 2016; Eveline et al. 2017). Grid refinement is often used near the fracture. Field scale production is estimated by multiplying the fracture-matrix element production with the number of elements (Jurus et al. 2013; Makhanov et al. 2014).

Shale gas adsorption affects storage, production and enhanced recovery (Rani et al. 2019; Klewiah et al. 2020). Cipolla et al. (2010) and Yu and Sepehrnoori (2014) simulated Barnett and Marcellus shale gas production accounting for gas desorption and reduced fracture conductivity under increasing closure stress. Gas desorption contributed to late time production while geomechanical effects had early negative impact. Sun et al. (2015) made similar conclusions on adsorption with a multiporosity model. Shale permeability can vary significantly with pressure (actually Knudsen number) (Florence et al. 2007; Darabi et al. 2012). Rubin et al. (2019) measured apparent permeability vs pressure and matrix compaction on Marcellus shale. Compaction was more dominant of the two and reduced field production estimates. Sun et al. (2015) argued that Knudsen effects were important on field scale. Berawala et al. (2019) and Berawala and Andersen (2020a) scaled shale gas production according to a dimensionless number stating how much matrix and fracture limited gas transport.

1.4. Simulation and field studies considering water

The hydraulic fracturing itself is not often modeled. A fracture-matrix geometry is assumed and water injection, flowback, shutin and production are simulated, during which water and gas production and in-situ saturation profiles in fracture and matrix are investigated (Holditch 1979; Ghanbari and Deghanpour 2016; Eveline et al. 2017; Elputranto and Akkutlu 2020). Jurus et al. (2013) captured the impact of fracturing to some extent by letting permeability increase at overpressure and reduce at depletion. They found that strong positive initial capillary pressures improved injectivity.

After fracturing, water occupies the fractures and begins to invade surrounding matrix. Capillary forces can drive spontaneous water uptake in porous media and resulting displacement in co- or counter-current direction of less wetting fluid (Liu et al. 2019; Andersen 2019). When trying to displace the water, the capillary forces hold on to the wetting fluid, especially near the matrix-to-fracture transition where capillary pressure approaches zero (Leverett 1941). The water entrapment and blockage near the fracture therefore depends on matrix wettability, amount of invasion and the magnitude of viscous and capillary forces (Richardson et al. 1952; Rapoport and Leas 1953).

Flowback can remove fracture water and limit matrix invasion. Gas production can be zero during a period of water production, seen e.g. for Woodford shale (Zhou et al. 2020). Subsequent shutin can benefit gas production if matrix water uptake draws water from the fractures and

fracture-matrix interface and returns gas towards the fractures. Several studies report reduced water rate and cumulative water production and increased gas rate after increased shutin time (Jurus et al. 2013; Bertoncello et al. 2014; Ghanbari and Deghanpour 2016; Fakcharoenphol et al. 2016; Lai et al. 2017; Zhang et al. 2017; Elputranto and Akkutlu 2020). Haynesville shale wells with low water recovery had high initial gas rates after fracturing (Fan et al. 2010). Cheng (2012) reported increased gas rate and reduced water rate after shutin compared to the initial period after fracturing for a Marcellus shale well. Ghanbari and Deghanpour (2016) analyzed wells from Horn River which were shut directly after fracturing and opened for production after 60 d. The wells were categorized into 'low water and high gas production' and 'high water and low gas production'. The former was associated with complex fracture network and large fracture-matrix contact surface where efficient spontaneous imbibition allowed significant uptake of water and gas filling the fractures. The latter was explained by a less complex network and less efficient replacement of water with gas in the fractures. Zhou et al. (2020) matched gas and water production from Woodford shale wells and cores. The overall gas permeability appeared to increase with water saturation as induced microfractures had greater effect than reduction of relative permeability. Imbibition and longer shutin time was suggested to improve gas production.

Cheng (2012), Jurus et al. (2013) and Fakcharoenphol et al. (2016) did not report significant impact of shutin time on long term gas production. Ghanbari and Deghanpour (2016) and Zhang et al. (2017) observed reduction with longer shutin time and argued that slow matrix transport can build up matrix water blockage. Bertoncello et al. (2014) matched well pressure for a known historical field gas production where gas rate was halved following shutin for a comparable well pressure. Water blockage reduced gas productivity, more with longer shutin or invasion. Eveline et al. (2017) assumed capillary imbibed water could be drawn into clay pores by osmosis, generating a swelling pressure that reduced permeability in the microfractures. They advocated for minimizing shutin time. Elputranto and Akkutlu (2020) reported that imbibition could occur during gas production due to strong capillary forces. Dynamic permeability changes were evaluated as less important than the water blockage.

1.5. Steady state modeling and this work

Once established, water blockage persists with time (Holditch 1979; Yao et al. 2019). Naik et al. (2018) calculated productivity reduction by water blockage using 1D steady state modeling of water and gas flow accounting for gas compressibility, Klinkenberg permeability and wettability alteration in mD-D permeability rock. Unlike their work we will consider tight rock with matrix compressibility, permeability reduction and compare production at a fixed drawdown, comparable with reservoir conditions. To our knowledge, this approach has not been used for tight rocks.
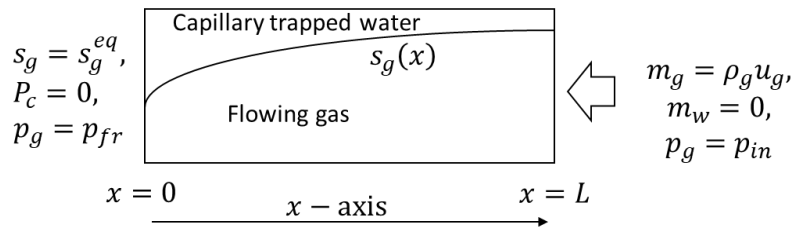
This work will consider the interplay between shale gas production and water blocking phenomena based on steady state flow, similar to Naik et al. (2018) for gas-water flow and Virnovsky et al. (1995) and Andersen et al. (2017, 2020) for core scale water-oil flow. The water invasion and blockage processes are in nature transient and must be treated such to account for shutin time, water volume and dynamic alterations of the matrix (e.g. osmosis and clay swelling). Shale is also better described with a multi-porosity formulation. Our approach hence does not fully

represent the water blockage phenomena. However, by studying the system under dynamic equilibrium conditions case comparison is simplified and key mechanisms are represented. We remind that generalization of our findings should be tested by including all relevant mechanisms in the system of interest. We focus on the matrix, similar to the dynamic modeling works Berawala and Andersen (2020b) and Elputranto and Akkutlu (2020). The fracture is represented via a known spacing and boundary conditions of pressure and (zero) capillary pressure. Mechanisms such as matrix-fracture pressure drawdown, (mixed) wettability, fluid tortuosity, rock and gas compressibility, permeability reduction and gas slippage are examined. The results are compared with having no water blockage. The theory is outlined in **Section 2**, we present numerical results in **Section 3** and we conclude the paper in **Section 4**.

2. Theory
2.1. Geometry
The scenario considered is 1D linear flow of gas at a fixed gas pressure drop along the matrix towards a natural or hydraulic fracture at $x = 0$ after water invasion. The gas pressure at $x = L$ is p_{in}, the gas pressure at the fracture is p_{fr} and the capillary pressure at the fracture is 0 (Leverett 1941). The mobile water that could flow has been displaced, but water blockage by capillary forces remains and the system is in steady state, see **Figure 1**. After deriving general transport equations, steady state allows to set time derivatives of local saturations and pressures to zero. A uniform mass flux m_g along the system is then calculated. The gas and porous medium are compressible, while water is incompressible. The phases are immiscible.

$$s_g = s_g^{eq},$$
$$P_c = 0,$$
$$p_g = p_{fr}$$

Capillary trapped water
$s_g(x)$
Flowing gas

$$m_g = \rho_g u_g,$$
$$m_w = 0,$$
$$p_g = p_{in}$$

$x = 0$
$x - \text{axis}$
$x = L$

Figure 1 Geometry of the system. Gas is flowing through the system according to a fixed pressure drop, entering from the right boundary $x = L$ while water is trapped by capillary forces. The saturation at the outlet $x = 0$ is fixed by the zero capillary pressure.

2.2. Mass conservation equations
The total mass of gas (in free and adsorbed form) in a small bulk volume dV_b is:

(1)	$$\phi s_g \rho_g dV_b + a_g \rho_r (1 - \phi_{in}) dV_b$$

where ϕ is porosity, s_g gas saturation, ρ_g gas density, a_g mass adsorbed gas per mass solid, ρ_r the (constant) mineral density. ϕ, ρ_g and a_g depend on gas pressure p_g. Porosity in the adsorption term is constant reflecting fixed adsorption capacity. Assuming the bulk volume has constant cross section and infinitesimal length dx, we obtain the following mass conservation equation:

(2)	$$\partial_t \left(\phi s_g \rho_g + a_g \rho_r (1 - \phi_{in}) \right) = -\partial_x (\rho_g u_g)$$

u_g is the Darcy gas velocity. Mass conservation for water can be derived as:

(3)	$$\partial_t(\phi \rho_w s_w) = -\partial_x(\rho_w u_w)$$

Water mass density ρ_w is constant. Water saturation s_w is related to gas saturation s_g by:

(4)	$$s_w + s_g = 1$$

2.3. Flux and permeability relations

The flux of gas is modelled assuming Darcy's law:

(5)	$$u_g = -\frac{K_a k_{rg}}{\mu_g}\partial_x p_g$$

K_a is apparent permeability, μ_g gas viscosity and k_{rg} relative permeability. Apparent permeability is defined by the product of intrinsic permeability K_∞ and a correction factor f dependent on the Knudsen number K_n (Karniadakis et al. 2002; Florence et al. 2007):

(6)	$$K_a = K_\infty f(K_n)$$
(7)	$$f(K_n) = (1 + \alpha_K K_n)\left(1 + \frac{4K_n}{1 + K_n}\right), \qquad \alpha_K = \frac{128}{15\pi^2}\tan^{-1}(4K_n^{0.4})$$

The Knudsen number K_n is the ratio of gas mean free flow path to pore radius defined as (Karniadakis et al. 2002):

(8)	$$K_n = \frac{\mu_g}{p_g r}\sqrt{\frac{\pi R T}{2 M_g}}$$

r is the characteristic pore radius, R the universal gas constant, M_g gas molecular weight, z real gas compressibility factor and T absolute temperature. Slip is important ($f > 1$) for large K_n.

Porosity and intrinsic permeability of shale can change due to compression or expansion, as driven by changes in pore pressure, confining stresses and temperature. Civan (2019) pointed out that several correlations for such relations have unrealistic limits at zero and infinite stress. Accounting for such limits and parameter changes before and after rock failure resulted in good description of experimental data. Pang et al. (2017) studied ~50 nD shale and found that adsorption affected porosity and permeability as the adsorption layer could fill significant parts of the pore space. They found that depressurization opened up more pore space than was closed by compression. For concept illustration we will use established exponential correlations (Dong et al. 2010; Guo et al. 2017):

(9)	$$\phi(p_g) = \phi_{in}\exp\left(-c_\phi(p_{g,in} - p_g)\right)$$
(10)	$$K_\infty(p_g) = K_{\infty in}\exp\left(-c_K(p_{g,in} - p_g)\right)$$

The index in refers to initial (reference) values. c_ϕ is the formation compressibility (under pore pressure changes only) and c_K expresses a similar dependence between intrinsic permeability and pore pressure changes. Guo et al. (2017) estimated from Carman-Kozeny theory that $c_K = 3c_\phi$, while Dong et al. (2010) measured $c_K > 10c_\phi$, both indicating that compression reduces

permeability more than porosity. Similarly, Ostermeier (2001) stated for ~1 D conglomerate rocks, that permeability reduction was 4-5 times higher than porosity reduction.

To estimate the pore radius r, we note that it can be related to permeability and porosity by bundle-of-tubes assumptions, as also applied by Jiang and Yang (2018), and obtain:

(11)	$$r = \sqrt{\frac{8\tau K_\infty}{\phi}}$$

where τ is tortuosity. Using the real gas equation we get gas density as function of pressure:

(12)	$$\rho_g = \frac{M_g}{RT} \frac{p_g}{z(p_g)}$$

The Peng and Robinson (1976) equation of state is used to calculate z:

(13)	$$z^3 - (1-B)z^2 + (A - 3B^2 - 2B)z - (AB - B^2 - B^3) = 0$$
(14)	$$A = 0.45724\, \alpha(T_r, \omega)\frac{p_r}{T_r^2}, \qquad B = 0.07780\frac{p_r}{T_r}, \qquad T_r = \frac{T}{T_{cr}}, \qquad p_r = \frac{p_g}{p_{cr}}$$
(15)	$$\alpha = \left(1 + \kappa(1 - T_r^{0.5})\right)^2, \qquad \kappa = 0.37464 + 1.54226\omega - 0.26992\omega^2$$

T_{cr}, p_{cr} and T_r, p_r are critical and reduced temperature and pressure and ω is the acentric factor. The largest real root for z is used.

2.4. Saturation functions

We assume connate water saturation equals residual water saturation ($s_{wc} = s_{wr}$). Gas is mobile for saturations given by:

(16)	$$s_{gr} < s_g < 1 - s_{wr}$$

Capillary pressure P_c is assumed to follow Leverett J-scaling (Dullien 2012; Bear 2013):

(17)	$$P_c(s_g) = p_g - p_w = \sigma_{gw}\sqrt{\frac{\phi}{K_\infty}}\, J(s_g)$$

$J(s_g)$ is the Leverett J-function. We assumed the intrinsic permeability in the scaling factor. Javadpour et al. (2007) performed mercury injection in tight shales (~50 to ~700 nD) and found capillary pressure curves 1-2 magnitudes higher than low permeable sand (0.23 mD) and limestone (4 mD), respectively, in line with the scaling.

Leverett (1941) stated that pressure continuity of phases flowing from a porous media into an open void (such as a fracture) enforces a zero capillary pressure boundary condition. Resulting, the saturation at that boundary is the one giving the capillary pressure function a zero value, denoted s_g^{eq}. A modified correlation by Bentsen and Anli (1976) is selected for the J-function as it can fit experimental data and has few tuning parameters J_1, J_2, s_g^{eq}:

(18)	$$J(s_g) = -J_1 \ln\left(\frac{1 - s_{wr} - s_g}{1 - s_{wr} - s_g^{eq}}\right) + J_2 \ln\left(\frac{s_g - s_{gr}}{s_g^{eq} - s_{gr}}\right)$$

For arbitrary (positive) values of these tuning parameters the curve goes to negative infinity at $s_g = s_{gr}$, positive infinity at $s_g = 1 - s_{wr}$ and zero at $s_g = s_g^{eq}$. For a strongly water-wet matrix $s_g^{eq} \approx s_{gr}$. The saturation derivative follows directly:

(19)	$$J'(s_g) = \frac{J_1}{1 - s_{wr} - s_g} + \frac{J_2}{s_g - s_{gr}}$$

The relative permeability of gas is assumed to follow a Corey type equation (Brooks and Corey 1966):

(20)	$$k_{rg}(S_g) = k_{rg}^{max} \left(\frac{S_g - S_{gr}}{1 - S_{wr} - S_{gr}} \right)^{n_g},$$

The Corey exponent n_g is usually set constant, but for a compacting porous medium the flow paths can meet more resistance. Yassin et al. (2016) found that a saturation tortuosity exponent of 3 gave a better match for shale than Wyllie and Gardner's (1958) choice of 2 for conventional media (this exponent is not the same as the Corey exponent n_g which combines all effects). To account for increased phase tortuosity we assume n_g has a fixed part $n_{g,in}$ (the value at reference conditions) and a part increasing with compaction:

(21)	$$n_g = n_{g,in} + \Delta n_g \left(1 - \frac{K_\infty}{K_{\infty,in}} \right).$$

2.5. Boundary conditions
The boundary conditions at the outlet $x = 0$ are given by a specified outlet / fracture pressure p_{fr} and a zero capillary pressure (i.e. a fixed saturation):

(22)	$$p_g(x = 0) = p_{fr}, \qquad P_c(x = 0) = 0, \qquad s_g(x = 0) = s_g^{eq}$$

The boundary condition at the other side is a constant gas pressure set equal to the reference pressure of the formation:

(23)	$$p_g(x = L) = p_{in}$$

2.6. Steady state description
At steady state, time derivatives are zero which from (2) and (3) gives uniform mass fluxes:

(24)	$$d_x m_g = 0, \qquad d_x m_w = 0$$

We also assume only gas is flowing, while any mobile water is trapped, meaning the water flux is zero, $m_w = 0$. That implies the water pressure gradient is zero at steady state, i.e. $d_x p_w = 0$. From the definition of capillary pressure in (17) it follows that:

(25)	$$d_x p_g = d_x P_c$$

With the definition of Leverett scaling and using that J is a function of saturation we get:

(26)	$$d_x p_g = \sigma_{gw} \sqrt{\frac{\phi}{K_\infty}} J'(s_g) d_x s_g$$

Gas has uniform (constant) mass flux $m_g = \rho_g u_g$. As density ρ_g varies according to pressure, so will Darcy velocity u_g. The gas pressure gradient follows from Darcy's equation, and the

saturation gradient follows by substituting the Darcy equation in (26). Further, we scale the spatial axis against the considered interval, $X = \frac{x}{L}$ and introduce the mass flux notation:

(27)	$$d_X p_g = -(L m_g \mu_g) \frac{1}{\rho_g K_g}$$
(28)	$$d_X s_g = -\left(\frac{L m_g \mu_g}{\sigma_{gw}}\right) \frac{1}{\rho_g K_g \sqrt{\frac{\phi}{K_\infty}} J'(s_g)}$$

Apart from L, μ_g, σ_{gw} and m_g the other parameters vary (spatially) according to functional relations with gas pressure or gas saturation: $K_g(p_g, s_g), \rho_g(p_g), \phi(p_g), K_\infty(p_g), J'(s_g)$ as defined by (6) to (21). Distributions of pressure and saturation are found by numerical integration of (27) and (28) starting with their fixed values at the outlet, see (22). The flux m_g is tuned to yield the correct pressure at $x = L$, see (23). The procedure is outlined in **Appendix A**. An implicit Euler method is implemented in Matlab. See **Appendix B** for a numerical validation of the model against Eclipse 100.

3. Results and discussion
3.1. Input parameters and relations
As our reference case we consider parameters in **Table 1** from Marcellus shale, as history matched by Yu et al. (2014) in terms of intrinsic permeability, fracture pressure (assumed well pressure), formation pressure, porosity, gas viscosity, temperature and fracture half spacing. Gas properties $(M_w, T_{cr}, P_{cr}, \omega)$ were based on methane. For multiphase flow parameters, water-methane interfacial tension was taken from Schmidt et al. (2007), gas relative permeability and saturation end points from Dacy (2010) and (scaled) capillary pressure from Byrnes (2011) (rescaled from experimental porosity and permeability, using (17)). Δn_g was set 0 for reference, but varied later. Rock compressibility parameters c_ϕ, c_K are shown in **Table 2** based on Dong et al. (2010) with low to high values selected spanning their observations for silty Chinshui shale. The LO case c_K also corresponds to data from Rubin et al. (2019) for Marcellus shale. The LO case c_ϕ is higher than the total compressibility in Yu and Sepehrnoori (2014) for Marcellus. We consider zero compressibilities (INC case) as reference.

Table 1 Input parameters used as base case in the simulations taken from 1: Yu et al. (2014), 2: Edwards and Celia (2018), 3: Evans and Civan (1994), 4: Schmidt et al. (2007), 5: Dacy (2010) and 6: Byrnes (2011). Δs_g^{eq} denotes $s_g^{eq} - s_{gr}$.

	Gas / rock properties		Multiphase properties		Other parameters
$^1 p_{in}$	$33 \cdot 10^6$ Pa	$^5 s_{gr}$	0.11	R	8.314 J/K/mol
$^1 p_{fr}$	$3.7 \cdot 10^6$ Pa	$^5 s_{wr}$	0.19	$r(p_{in})$	12 nm = $1.2 \cdot 10^{-8}$ m
$^1 k_{\infty,in}$	$600\, nD = 6 \cdot 10^{-19}$ m^2	$^5 k_{rg}^{max}$	0.435	τ	2
$^1 \mu_g$	$2.0 \cdot 10^{-5}$ Pa s	$^5 n_{g,in}$	5.0	P_{cr}	4.5992 MPa
$^1 L$	15 m	Δn_g	0	T_{cr}	190.56 K
$^1 T_{res}$	352 K	$^6 \Delta s_g^{eq}$	0.001	ω	0.011

[1]ϕ_{in}	0.065	[6]J_1	0.5		
[2]M_g	$16.04 \cdot 10^{-3}$ kg/mol	[6]J_2	0.03		
[4]σ_{gw}	0.050 N/m				

Table 2 Compressibility parameters for different cases. The low, medium and high values are reported in Dong et al. (2010) for Chinsui shale. The LO c_K also corresponds to Marcellus shale from Rubin et al. (2019).

Case	INC	LO	MED	HI
c_ϕ	0 Pa^{-1}	$0.4 \cdot 10^{-9}$ Pa^{-1}	$1.0 \cdot 10^{-9}$ Pa^{-1}	$1.3 \cdot 10^{-9}$ Pa^{-1}
c_K	0 Pa^{-1}	$15 \cdot 10^{-9}$ Pa^{-1}	$25 \cdot 10^{-9}$ Pa^{-1}	$43 \cdot 10^{-9}$ Pa^{-1}
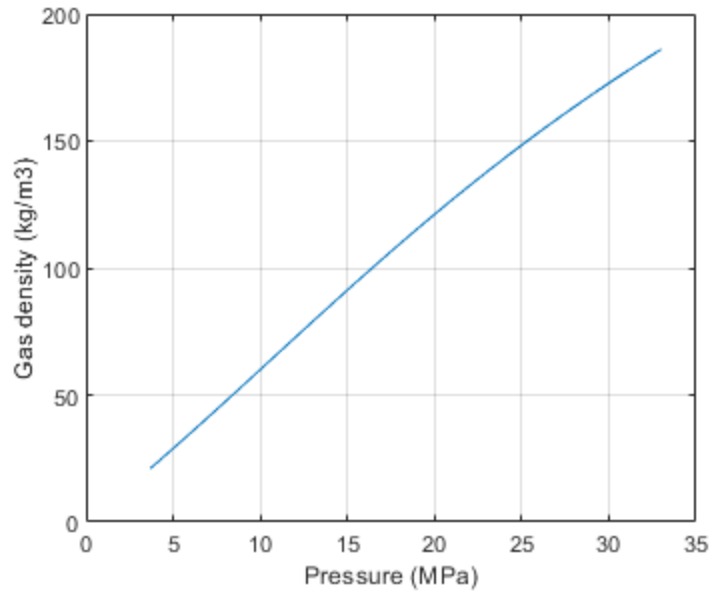
Figure 2 Gas density vs pressure at T_{res}.

Gas density at T_{res} is plotted vs pressure in **Figure 2**. Density is seen to reduce by a factor of ~10 from p_{in} to p_{fr} (the highest and lowest pressure, respectively). Porosity and permeability are shown in **Figure 3a** and **b**, respectively, for different compressibility cases according to **Table 2**. For the most compressible case (HI) porosity reduces from 0.065 at initial state $p_{in} = 33$ MPa to 0.0626 at the lowest pressure p_{fr} (a reduction by factor 0.963). Intrinsic permeability K_∞ reduces more significantly with pressure by as much as 0.25 of the initial value (600 nD at p_{in}) for the most compressible case.

The importance of slip increases when pore radius decreases or pressure decreases (Florence et al. 2007; Darabi et al. 2012). As we consider nanoporous media, gas slip is significant and causes apparent permeability to be higher than intrinsic permeability for all the considered pressures and cases in **Figure 3b**. For the incompressible rock case, apparent permeability increases with lower pressure and reaches over twice the value of the constant intrinsic permeability at the lowest pressure. For more compressible cases, the reduction of pore radius with intrinsic permeability makes slip more important. The ratio of apparent to intrinsic permeability increases (towards a factor 3 at the lowest pressure for the most compressible case). Apparent

permeability profiles with pressure are seen to reduce with higher compressibility. Rubin et al. (2019) measured apparent to intrinsic permeability ratios towards 2 for Marcellus shale, consistent with these ranges. Darabi et al. (2012) stated the ratio could be 10 for nanopores. Gas relative permeability is shown in **Figure 4a** with variations of gas Corey exponent n_g. Scaled and unscaled capillary pressure is shown in **Figure 4b** with variations of Δs_g^{eq}.
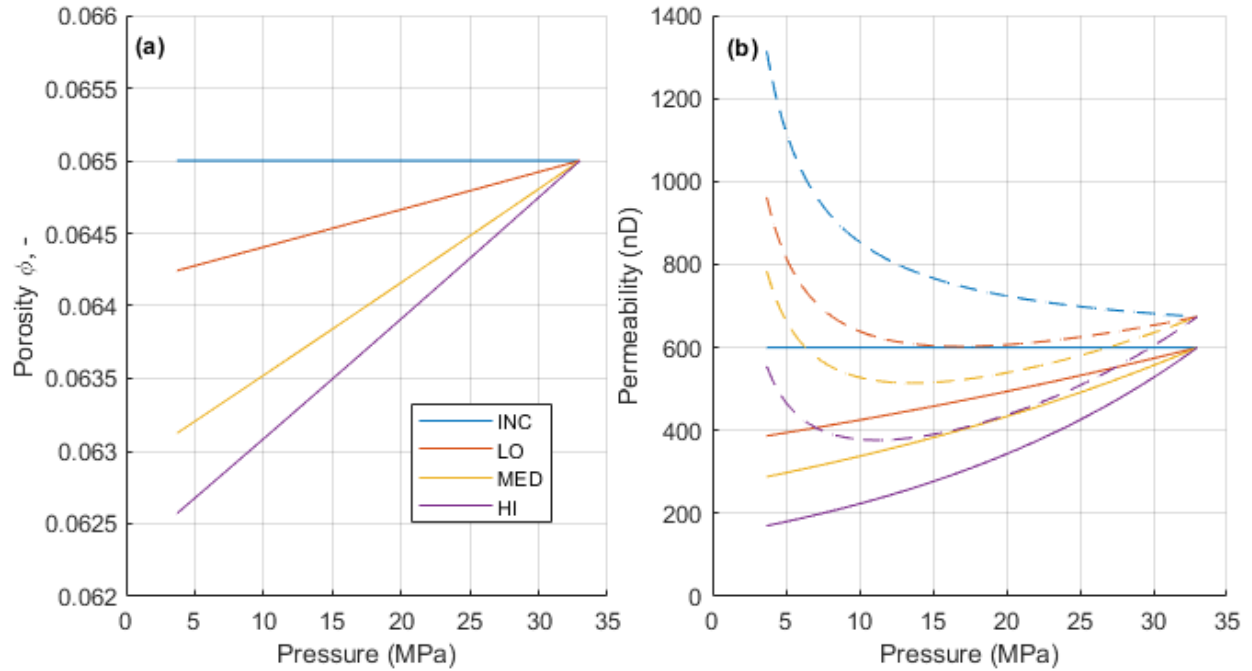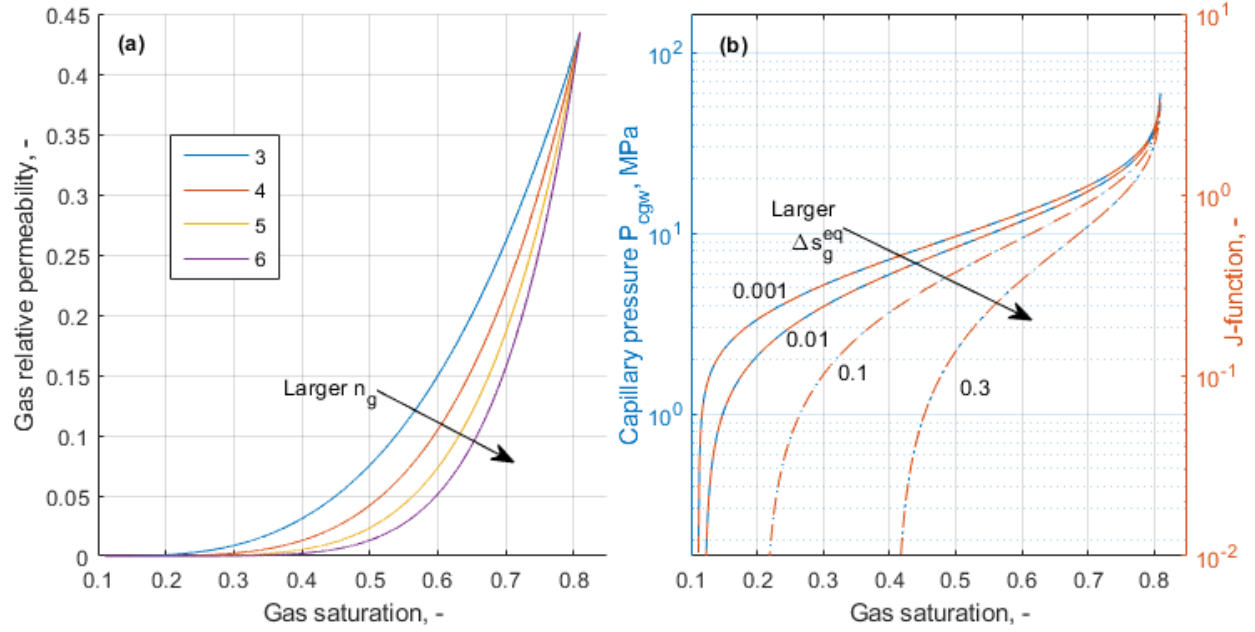

Figure 3 Porosity (a) and permeability (b) vs pressure for different compressibility cases (INC, LO, MED, HI) with parameters from Table 2. Full and dashed lines in (b) indicate intrinsic and apparent permeability, respectively.

Figure 4 Gas relative permeability (a) for different Corey exponents n_g (5 is the reference). Also (b) scaled and unscaled water-gas capillary pressure based on a rescaled mercury drainage curve from **Byrnes (2011)** to residual water and gas saturations from **Dacy (2010)**. The cross over saturation has been varied using different Δs_g^{eq} (values indicated) where 0.001 corresponds to the experimental data.

3.2. Model outputs

In the examples, pressure varies between defined values $p_g(x = 0) = p_{fr}$ and $p_g(x = L) = p_{in} = 33$ MPa (reference). The resulting gas mass flux m_g is reported. We investigate the role of pressure drawdown $\Delta P = p_{in} - p_{fr}$ (with p_{in} fixed), saturation functions by changing $\Delta s_g^{eq} = s_g^{eq} - s_{gr}$ or Corey exponent n_g, shale compressibility (via c_ϕ and c_K as in **Table 2**), and saturation tortuosity Δn_g. The model calculates spatial saturation and pressure distributions. Results with blocking ('WB') and without ('NBL') are compared. If no blocking is present, gas saturation is set uniform to $s_g(x) = 1 - s_{wr}$. Then saturation functions do not have impact, but the pressure gradient can depend on porosity, permeability, etc. We report distributions of:

- Normalized gas saturation: $\frac{s_g(x) - s_{gr}}{1 - s_{wr} - s_{gr}}$ (equals 0 at $s_g = s_{gr}$ and 1 at $s_g = 1 - s_{wr}$)

- Normalized gas pressure: $\frac{p_g(x) - p_{fr}}{p_{in} - p_{fr}}$ (equals 0 at $x = 0$ and $p_g = p_{fr}$ and 1 at $x = L$ and $p_g = p_{in}$)

- Apparent permeability: $K_a(x)$

Porosity is not shown since the applied data do not suggest greater reduction than a factor 0.963.

3.3. Formation drawdown and gas flow mechanisms

In **Figure 5** results are shown where the drawdown ΔP has been varied from the reference to lower values by increasing the fracture pressure p_{fr}. That can be a result of higher well pressure or that the fractures have low conductivity and there is a significant pressure loss along the fracture to the

well. Significant water accumulation is observed for the four pressure drops. For the reference case (relative drawdown 1, blue curves) water occupies 10-15% of the volume mobile gas could occupy. Lower drawdown of 0.76, 0.52 or 0.34 of the reference value, lets capillary forces dominate more and hold a higher amount of water in the matrix. Assuming saturation and pressure profiles are calculated, we note that integration of (25) the local capillary pressure will be related to gas pressure as:

(29)	$$P_c(x) = p_g(x) - p_{fr}$$

Hence, it is zero at the fracture and increasing away from it until $P_c = \Delta P$ at $x = L$. Higher pressure drawdowns therefore allow greater magnitude capillary pressure distributions, and thus higher gas saturations, according to the $P_c(s_g)$ relations seen in **Figure 4b**. The trapped water is mainly accumulated at the outlet $x = 0$ where the gas saturation profiles converge to s_g^{eq}, see **Figure 5a**. Steeper saturation gradients and wider saturation intervals are obtained for higher pressure drop. For no water blockage (NBL), a flat saturation profile is seen in **Figure 5b**.

Most of the pressure drop occurs over the water blockage zone where gas relative permeabilities are reduced, see **Figure 5c**. 45% of the pressure drop happens within 5% of the system length at the largest drawdown, while it is 65% for the least drawdown. Essentially, lower pressure drop allows more blockage to occur, thus low drawdown both gives lower driving force for gas production and a less efficient process. It is worth noting that the saturation range of each profile in **Figure 5a** corresponds to the capillary pressure range from 0 to ΔP for that case. The NBL cases in **Figure 5d** show more linear pressure profiles (than the WB cases), but still with higher pressure drop downstream. For relative drawdown 1, 10% of the pressure drop occurs over the 5% length closest to the fracture while it approaches 5% for less drawdown. To explain this we consider the pressure gradient relation in (27). The pressure gradient increases if gas permeability decreases or gas density decreases (increasing the Darcy velocity and the pressure gradient proportionally) for stable mass flux conditions. Apparent permeability increases gradually with lower pressure, seen in **Figure 5f**. However, density decreases strongly towards the outlet for the reference case, consider **Figure 2**. The two effects work oppositely, but the gas expansion is dominant. When the drawdown is low, both apparent permeability and density change less from the initial value, giving a more constant pressure gradient.

For the WB cases, upstream pressure is maintained at a high level resulting in little variation of K_a (and ρ_g) before the sharp pressure gradient zone near the outlet ($x < {\sim}0.1$). These cases have more compact K_a profiles than their corresponding NBL cases, see **Figure 5e**. However, the density reduction near the outlet increases the Darcy velocity and pressure gradient which may be positive for removing blockage.
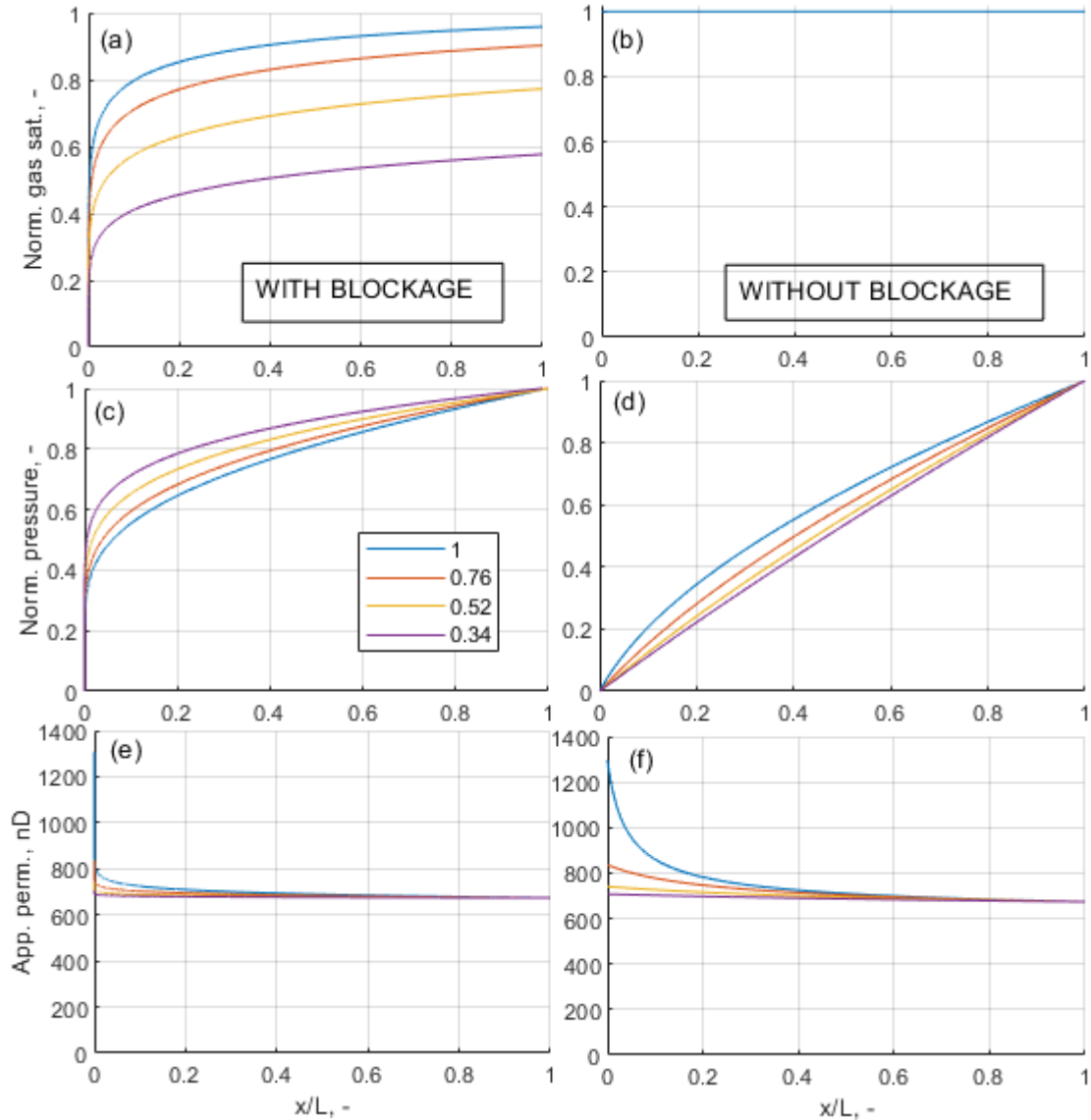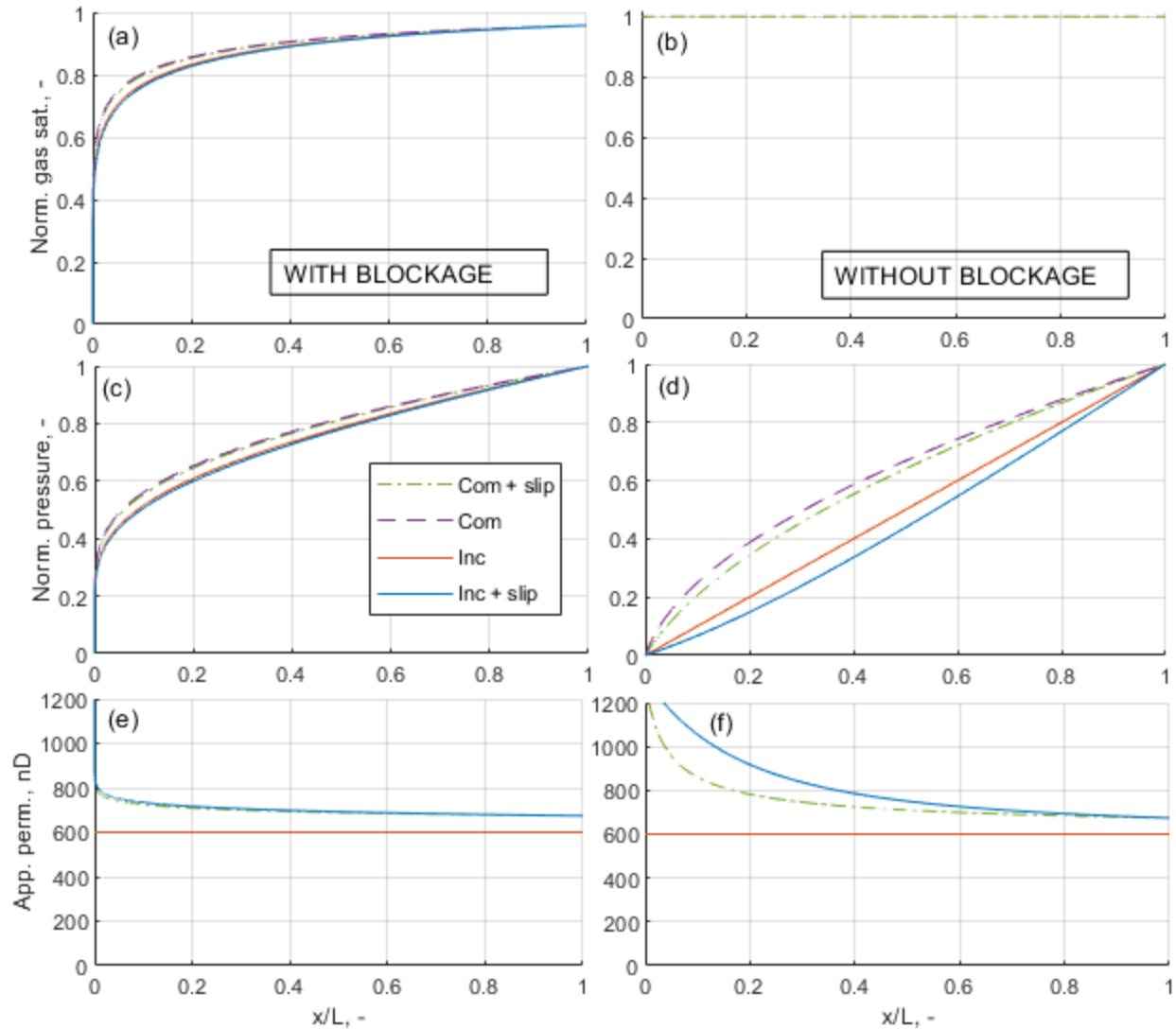
Figure 5 Normalized gas saturation (a,b), normalized pressure (c,d) and apparent permeability (e,f) spatial distributions for different relative drawdowns $\left(\frac{\Delta P}{\Delta P_{ref}}\right)$, varied using p_{fr}. Other parameters are kept at reference values. Water blockage is accounted for in the left figures but not in the right.

To investigate how slip and gas compressibility interact, the reference case was modified by setting gas density constant based on initial formation pressure and apparent permeability equal to intrinsic permeability: $\rho_g = \rho_g(p_{in}), K_a = K_\infty$. Resulting spatial profiles are shown in **Figure 6**.

For NBL cases, if the gas is incompressible and there is no slip, the pressure gradient is constant and a linear pressure profile is obtained, see **Figure 6d**. Adding slip gives more pressure drop upstream because of the elevated permeability at low pressures downstream. Compressibility gives more pressure drop downstream since the Darcy velocity increases. This changes the profiles more than slip because density reduces by a factor ~10 (**Figure 2**) while apparant permeability increases by a factor ~2 (**Figure 3b**) over the pressure reduction. Apparent permeability, see

Figure 6f, is highest for the incompressible case with slip since the pressure gradient is highest upstream, giving generally lower pressures and higher permeability.

The same variations of K_a and ρ_g with pressure take place for the WB cases, but blockage shifts the pressure drop towards the fracture. Scaled saturation (**Figure 6a**) and pressure profiles (**Figure 6c**) overlap more according to whether gas is compressible or not than whether the slip factor is 1 or not. The compressibility effect increases the pressure gradient in the blockage zone and causes more water displacement than if gas is assumed incompressible.

Figure 6 Normalized gas saturation (a,b), normalized pressure (c,d) and apparent permeability (e,f) spatial distributions where gas is either compressible ('Com') or not ('Inc') and slip is accounted for ('slip') or not for the reference case. Water blockage is accounted for in the left figures but not in the right.

The mass fluxes were calculated for each case and are summarized in **Table 3**. For NBL cases, the lowest mass flux $\left(2.8 \cdot 10^{-6}\, \frac{\text{kg}}{\text{m}^2\text{s}}\right)$ is obtained when gas is compressible (high pressure gradient when gas expands) and slip not accounted for (lower permeability). The highest flux

$\left(6.2 \cdot 10^{-6} \frac{\text{kg}}{\text{m}^2\text{s}}\right)$ resulted when gas was assumed incompressible and slip included. Slip increased the flux by 23 and 32 % in the compressible and incompressible case, respectively. The same trends were observed for the WB cases although there was less variation in fluxes. The lowest flux (compressible, no slip) was $1.2 \cdot 10^{-6} \frac{\text{kg}}{\text{m}^2\text{s}}$ and the highest (incompressible, with slip) was $1.7 \cdot 10^{-6} \frac{\text{kg}}{\text{m}^2\text{s}}$. Slip increased the mass flux by 16 % for both incompressible and compressible cases. This is comparable to Sun et al.'s (2015) findings that slip increased production by 23 %.

Table 3 Calculated gas mass fluxes for the reference case where gas compressibility and slip assumptions are modified.

		m_g (kg/m2/s)	m_g^{NBL} (kg/m2/s)
Compressible gas	Slip	1.4E-06	3.4E-06
Compressible gas	No slip	1.2E-06	2.8E-06
Incompressible gas	Slip	1.7E-06	6.2E-06
Incompressible gas	No slip	1.5E-06	4.7E-06

3.4. Wettability and flux relations

The impact of wettability is explored by varying Δs_g^{eq} which shifts the capillary pressure curve (see **Figure 4**) to less water-wet for higher Δs_g^{eq}. The impact on spatial distributions is shown in **Figure 7**. Increasing Δs_g^{eq} from 0.001 (reference) towards 0.3, the capillary pressure is lowered and effectively holds less strongly onto the water phase and on a smaller saturation interval. From (29) the capillary pressure will cover the same range for all these cases, but higher gas saturations are obtained for a given capillary pressure in less water-wet cases. The given pressure drop is thus able to displace more of the water, which further increases the gas relative permeability. The blockage becomes less dominant on the pressure drop and gives a more even pressure profile approaching the NBL case. This is consistent with the role of wettability and viscous forces on water blocking as commented in other works (Naik et al. 2018; Andersen et al. 2020; Elputranto and Akkutlu 2020).
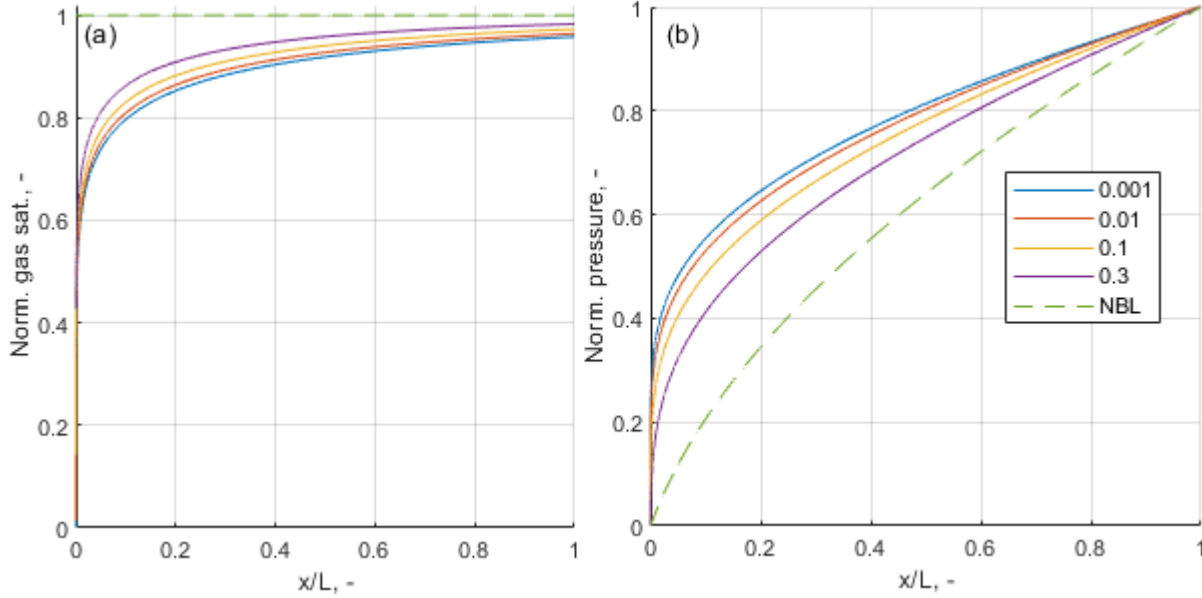
Figure 7 Spatial distributions of normalized gas saturation (a) and normalized pressure (b) for different wetting states, according to the indicated value of $\Delta s_g^{eq} = s_g^{eq} - s_{gr}$ (low values means more water-wet). The corresponding case with no water blockage (NBL) is indicated with dashed line.

Calculated mass fluxes m_g are plotted against drawdown for each wetting state (given by Δs_g^{eq}) and the NBL case in **Figure 8a**. A consistently higher flux is obtained when the drawdown is increased and the matrix is less water-wet (higher Δs_g^{eq}). The mass fluxes increase close to linearly with drawdown at high drawdowns, but at low drawdowns the more water-wet case fluxes decline rapidly towards very low values as water blockage reduces the mobile gas saturations. Mobile gas saturations are necessary for flow to occur. For strongly water-wet cases low drawdowns confine this saturation range very narrowly around the critical gas saturation which is why the fluxes become so low. For strongly water-wet cases, once drawdown is less than the capillary threshold pressure, saturations vary little and the blockage is close to complete. This is seen as very small fluxes for drawdown less than 8 MPa in the examples with $\Delta s_g^{eq} = 0.001$ and 0.01. Conditions for complete blockage were also discussed by Holditch (1979) and Yao et al. (2019).

In **Figure 8b** is plotted the NBL flux divided by the WB fluxes for the different wetting states against relative drawdown $\Delta P / \Delta P_{ref}$. The trends show that gas production influenced by blockage is extremely sensitive to drawdown. At the reference drawdown the rates are reduced by water blockage with factors 1.5-3 compared to if there was no blockage. Halving the drawdown reduces the rate by factors 3.5-15 compared to no blockage rates. A higher drawdown increases the rate both by increasing the driving force and reducing the blockage. A less water-wet system has less blockage.
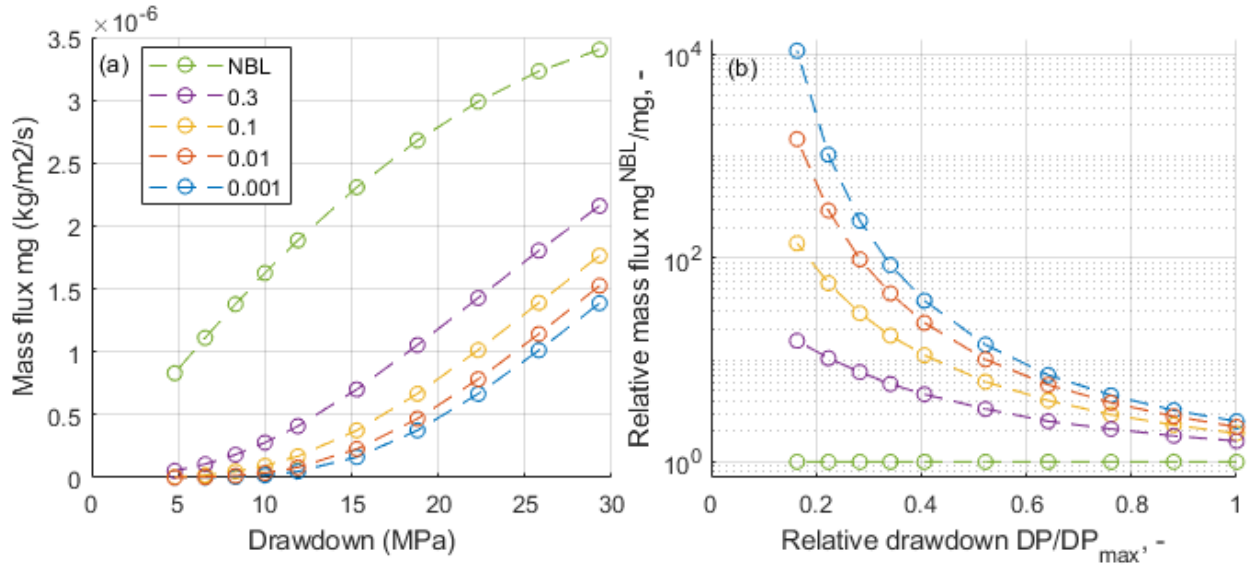
Figure 8 Mass flux m_g vs drawdown $\left(\Delta P = P_{in} - P_{fr}\right)$ (a) for the case with no water blockage (NBL) and blockage cases with different wetting indicated by $\Delta s_g^{eq} = s_g^{eq} - s_{gr}$ (lower value means more water-wet). Relative fluxes on log scale for the same cases (how high flux is obtained without blockage compared to with blockage) are plotted in (b) against relative drawdown $(\Delta P/\Delta P_{ref})$.

3.5. Corey exponent

The role of gas Corey exponent n_g is illustrated in **Figure 9**. Low gas relative permeability (high n_g) implies that gas flow carries a greater viscous force at a given flux, but also has more resistance to flow. These effects combined lead to increased gas saturations (for higher n_g) while at the same time more of the pressure loss takes place near the outlet. Despite the reduced blockage in terms of higher gas saturations, the gas mass fluxes are reduced with increasing n_g, see **Table 4**. Blockage reduces the flux with a factor 2.75 at Corey exponent 6 and a factor 1.89 at Corey exponent 3.
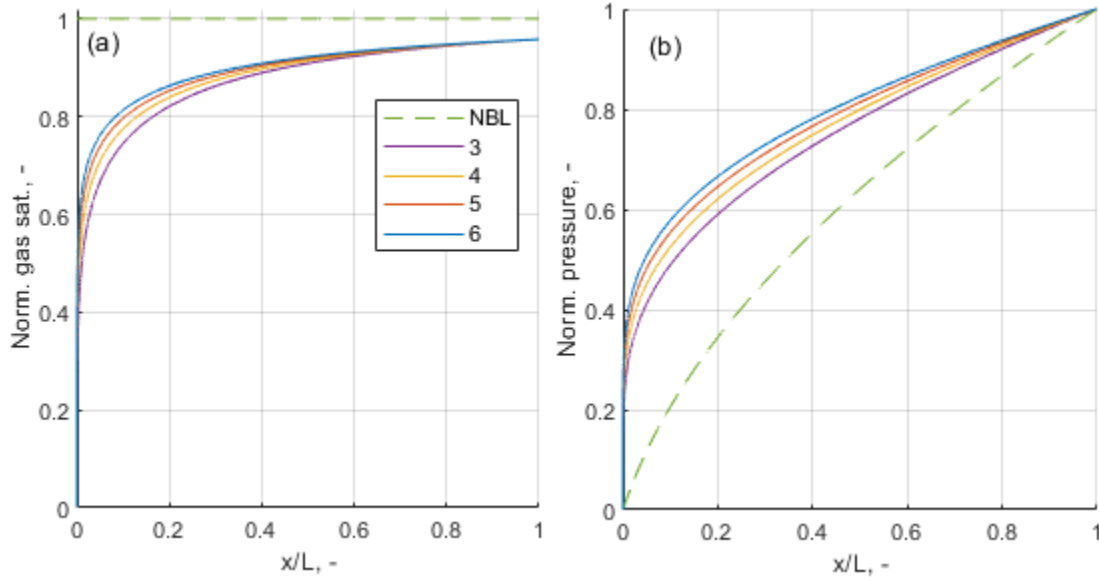
Figure 9 Spatial distributions of normalized gas saturation (a) and normalized pressure (b) for different gas Corey exponents (values indicated) for the reference case. The corresponding case with no water blockage (NBL) is indicated with dashed line.

Table 4 Calculated gas mass fluxes and how much they are lowered by blockage for different gas Corey exponents in the reference case.

Gas Corey exponent n_g	Gas flux m_g (kg/m2/s)	Gas flux m_g^{NBL} (kg/m2/s)	m_g^{NBL}/m_g
3	1.79E-06	3.401E-06	1.89
4	1.57E-06	3.401E-06	2.17
5	1.39E-06	3.401E-06	2.45
6	1.24E-06	3.401E-06	2.75

3.6. Shale compressibility

Shale compressibility is varied using the cases listed in **Table 2**. The results are seen in **Figure 10**. Since the pressure interval is the same (from 33 to 3.7 MPa), a given compressibility case yields the same porosity and permeability range for WB and NBL cases. For WB cases most of the pressure drop occurs near the outlet: more than 50 % of the pressure drop occurs within the 10 % length nearest the fracture for all cases, see **Figure 10c**. Relatively high pressure is maintained upstream in the WB cases compared to the NBL cases for same compressibility (see **Figure 10d**). Thus compressibility had less impact on the pressure profiles than the water blockage, but it is seen that higher compressibility shifts more of the pressure drop towards the outlet. As we have seen in **Figure 3b** and also see in **Figure 10** for WB and NBL cases, the net effect of compressibility is to reduce apparent permeability. The INC case has higher pressure gradient near the fracture due to gas expansion dominating over slip, while higher compressibility reduces the apparent permeability profiles towards the outlet compared to the INC case. The relatively uniform pressures in the WB cases compared to the NBL cases result in a narrower range of apparent permeability profiles, compare **Figure 10e** and **Figure 10f**: at $\frac{x}{L} = 0.2$ the apparent permeability

ranges from 500 to 700 nD for WB cases, while the range is 400 to 800 nD for NBL cases. In this sense water blockage mitigates permeability reduction. Capillary pressure is also increased by compression and the added water blockage shifts more of the pressure drop towards the fracture and maintains pressure upstream. The increased capillary forces are also reflected in generally lower gas saturation profiles, see **Figure 10a**.

The mass fluxes for the different cases are shown in **Table 5** and generally display reduced production with higher compressibility, as explained by reduced permeability (for WB and NBL cases) and stronger capillary forces (for the WB case). The NBL gas flux is 1.5 times higher for the INC case compared to the HI case, while the WB gas flux is 2.4 times higher for the INC case compared to the HI case. Although the average reduction of permeability is less for the WB cases, the compressibility impact is greater on the production for these cases as explained by the raised capillary forces and more compressibility leads to greater impact of the water blockage: blockage gives a rate reduction of 2.5 for the INC case and 4.0 for the HI case.
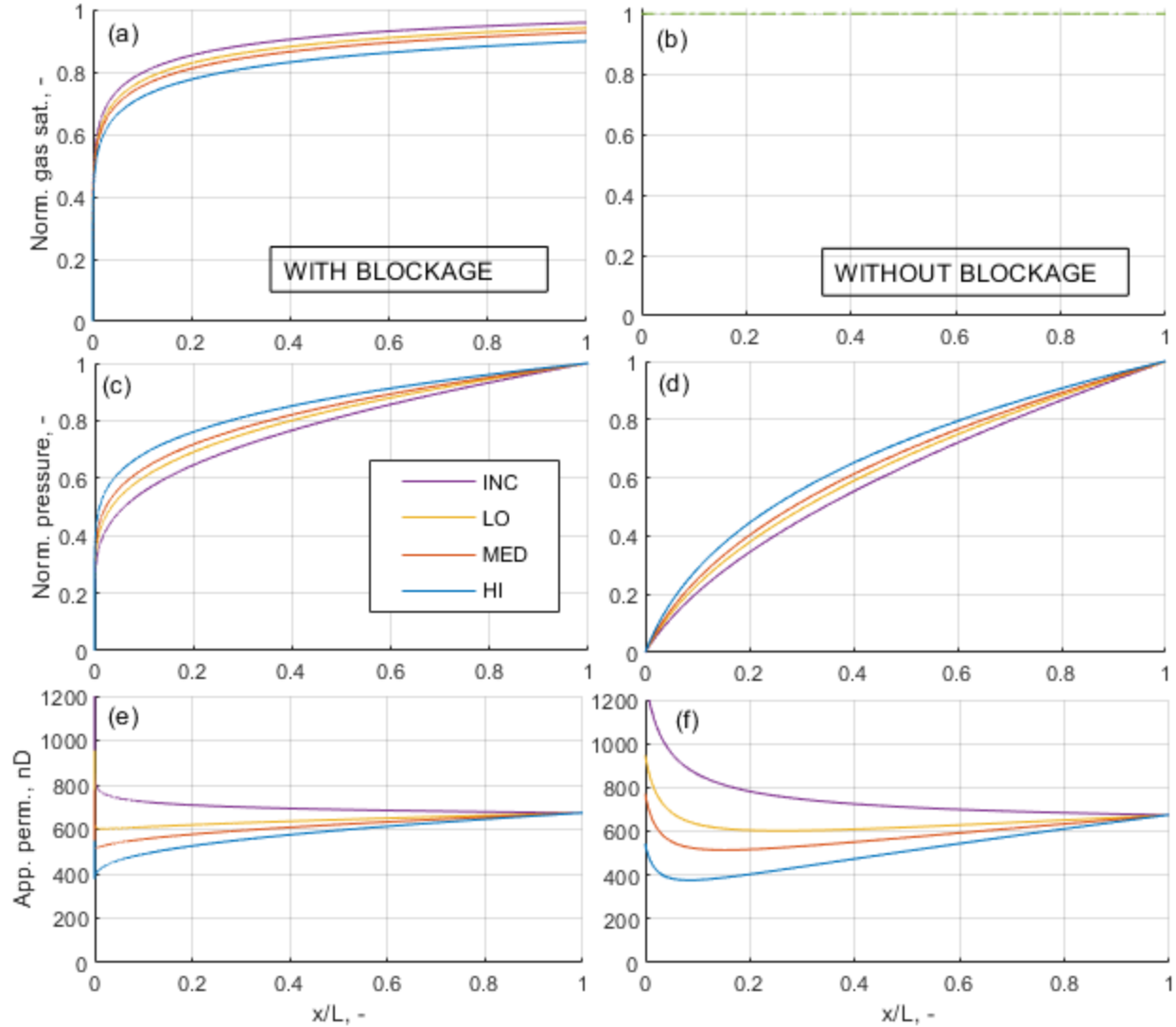
Figure 10 Normalized gas saturation (a,b), normalized pressure (c,d) and apparent permeability (e,f) spatial distributions for different compressibility cases (INC, LO, MED, HI). Water blockage is accounted for in the left figures but not in the right.

Table 5 Calculated gas mass fluxes with and without blockage and their ratio for different shale compressibilities in the reference case.

Shale compressibility c_{sh} (Pa-1)	Gas flux m_g (kg/m2/s)	Gas flux m_g^{NBL} (kg/m2/s)	m_g^{NBL}/m_g
INC	1.4E-06	3.4E-06	2.5
LO	1.0E-06	2.9E-06	2.9
MED	8.4E-07	2.7E-06	3.2
HI	5.7E-07	2.3E-06	4.0

3.7. Saturation tortuosity

When rock is compressed it is possible that the fluid flow paths become more complex, as reflected by lower relative permeabilities. The gas Corey exponent was assumed to increase with intrinsic

permeability reduction as given by (21) based on the parameter Δn_g. Assuming the HI compressibility case, results from varying Δn_g are shown in **Figure 11**. The declining pressure towards the outlet is accompanied by intrinsic permeability reduction and increasing Corey exponents. When Δn_g is higher, the Corey exponent increases more (from a base value of 5 towards 14 at the highest compression). Water blockage prevents a significant pressure drop upstream, see **Figure 11b**, hence changes in permeability and n_g are gradual upstream and they get sharp gradients near the outlet. As Δn_g increases gas mobility is reduced in the compressed region near the outlet and hence pressure and apparent permeability upstream ($\frac{x}{L} > {\sim}0.2$) become more uniform. The increased viscous force associated with gas flow reduces the water blockage, see the higher gas saturation profiles in **Figure 11a**. That is also related to how the maintained high pressure upstream prevents compression and increased capillary forces.

   The gas mass fluxes for the different cases are listed in **Table 6**. Saturation tortuosity reduces the gas production by a factor 0.69 when Δn_g goes from 0 to 12. Although the Corey exponent is allowed to be greatly increased (from 5 to 14 along the system for the highest Δn_g), the effect is local and water blockage is removed, counter-acting the reduced mobility at a given saturation.
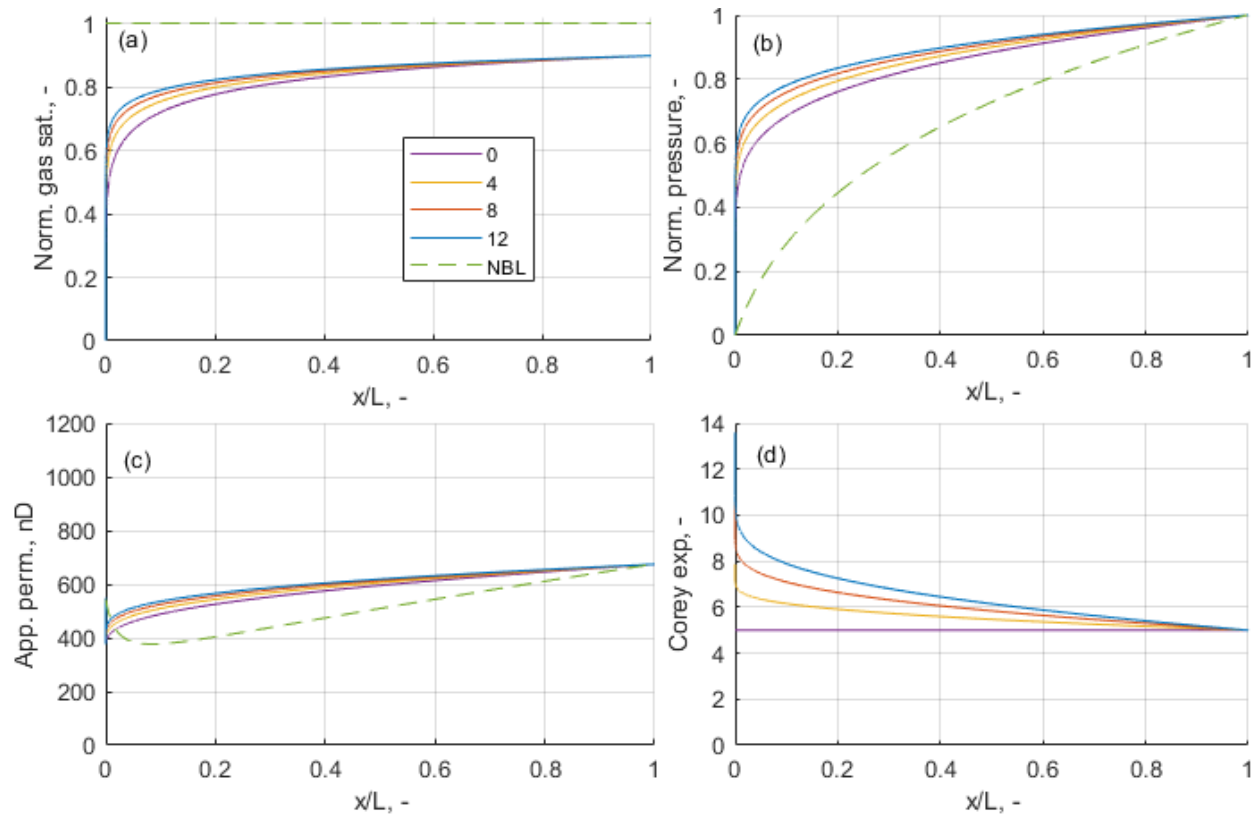
Figure 11 Normalized gas saturation (a), normalized pressure (b), apparent permeability (c) and gas Corey exponent (d) spatial distributions for different values of Δn_g considering the HI compressibility case. The coresponding case without water blockage (NBL) is shown in dashed line.

Table 6 Calculated gas mass fluxes with and without blockage and their ratio for different saturation tortuosities in the reference case assuming the HI compressibility case.

Saturation tortuosity Δn_g	Gas flux m_g (kg/m2/s)	Gas flux m_g^{NBL} (kg/m2/s)	m_g^{NBL}/m_g
0	5.74E-07	2.29E-06	3.99
4	4.94E-07	2.29E-06	4.64
8	4.38E-07	2.29E-06	5.23
12	3.96E-07	2.29E-06	5.79

4. Conclusions

A model was presented for steady state flow of compressible gas with water blockage in compressible shale subject to slippage, compaction-dependent permeability and saturation tortuosity. The steady state assumption relies on unlimited access to water and time which maydifferent from practical situations where a limited amount of fracturing fluid resides in the fractures and may imbibe during shutin some months before production.

Based on realistic input parameters for shale, sensitivity analyses of the model demonstrated that a significant amount of water can invade the matrix, be trapped by strong capillary forces and cannot be removed by the natural pressure driving forces of the formation. This underlines the importance of minimizing the fracture fluid loss to the formation.

There is a lot to gain in gas productivity and fracture fluid recovery by altering wettability to less water-wet, reducing capillary pressure (by interfacial tension) or keeping as high drawdown (pressure drop) as possible without damaging the fracture conductivity. The amount of fluid trapped and factor of rate reduction was very sensitive to pressure drop. Gas production rate reduced by a couple orders of magnitude just by reducing the drawdown 75% from the reference.

In addition to reducing relative permeability, water blockage causes the main pressure drop to occur near the outlet and hence maintain a high pressure upstream and centrally in the matrix. The high pressure limits slippage, gas and rock compressibility effects to occur more locally near the outlet compared to a no blockage system. Mechanisms increasing pressure drop at low pressure (gas and rock compressibility, saturation tortuosity) tended to give a steeper pressure gradient towards the outlet. This however reduced the interval where these effects were very significant and counteracted their impact. The added viscous force could displace more water, but the added resistance reduced gas production.

Physicochemical interactions such as osmosis or clay swelling were not considered. Stresses induced by clay swelling could lead to permeability reduction (Eveline et al. 2017; Elputranto and Akkutlu 2020).

Nomenclature
Roman

a_g	Adsorbed gas, kg/kg
c_ϕ	Porosity formation compressibility, Pa^{-1}
c_K	Permeability formation compressibility, Pa^{-1}
K_a	Apparent permeability, m^2

K_∞	Intrinsic permeability, m^2
K_g	Effective gas permeability, m^2
k_{rg}	Gas relative permeability, -
K_n	Knudsen number, -
m_g	Mass gas flux, kg/m^2/s
M_g	Gas molecular weight, kg/kgmol
p_i	Phase pressure, Pa
R	Gas constant, J/K/mol
r	Pore radius, m
s_i	Phase saturation, -
S_g	Normalized gas saturation, -
s_{ir}	Irreducible phase saturation, -
z	Real gas compressibility factor, -

Greek

ρ_i	Phase mass density, kg/m^3
ρ_r	Rock mass density, kg/m^3
μ_i	Phase viscosity, Pa s
ϕ	Porosity, -

Indices

c	Capillary
cr	Critical
fr	Fracture
g	Gas
i	Phase
in	Initial / reference state
r	Rock
w	Water

References

1. Andersen, P. Ø., Standnes, D. C., & Skjæveland, S. M. (2017). Waterflooding oil-saturated core samples-Analytical solutions for steady-state capillary end effects and correction of residual saturation. *Journal of Petroleum Science and Engineering*, *157*, 364-379.

2. Andersen, P. Ø. (2019). A simplified modelling approach for petroleum recovery by spontaneous imbibition in naturally fractured reservoirs. *Journal of Natural Gas Science and Engineering*, *63*, 95-114.

3. Andersen, P. Ø., Walrond, K., Nainggolan, C. K., Pulido, E. Y., & Askarinezhad, R. (2020). Simulation Interpretation of Capillary Pressure and Relative Permeability From Laboratory Waterflooding Experiments in Preferentially Oil-Wet Porous Media. *SPE Reservoir Evaluation & Engineering*, *23*(01), 230-246.

4. Bear, J. (2013). *Dynamics of fluids in porous media*. Courier Corporation.

5. Bentsen, R. G., & Anli, J. (1976). A new displacement capillary pressure model. *Journal of Canadian Petroleum Technology*, *15*(03).

6. Berawala, D. S., Andersen, P. Ø., & Ursin, J. R. (2019). Controlling Parameters During Continuum Flow in Shale-Gas Production: A Fracture/Matrix-Modeling Approach. *SPE Journal*.

7. Berawala, D. S., & Andersen, P. Ø. (2020a). Numerical investigation of Non-Darcy flow regime transitions in shale gas production. *Journal of Petroleum Science and Engineering*, 107114.

8. Berawala, D. S., & Andersen, P. Ø. (2020b). Evaluation of Multicomponent Adsorption Kinetics for Carbon Dioxide Enhanced Gas Recovery from Tight Shales. *SPE Reservoir Evaluation & Engineering*.

9. Bertoncello, A., Wallace, J., Blyton, C., Honarpour, M., & Kabir, C. S. (2014, February). Imbibition and water blockage in unconventional reservoirs: well management implications during flowback and early production. In *SPE/EAGE European unconventional resources conference and exhibition* (Vol. 2014, No. 1, pp. 1-13). European Association of Geoscientists & Engineers.

10. Borysenko, A., Clennell, B., Sedev, R., Burgar, I., Ralston, J., Raven, M., ... & Liu, K. (2009). Experimental investigations of the wettability of clays and shales. *Journal of Geophysical Research: Solid Earth*, *114*(B7).

11. Brooks, R. H., & Corey, A. T. (1966). Properties of porous media affecting fluid flow. *Journal of the irrigation and drainage division*, *92*(2), 61-90.

12. Byrnes, A. P. (2011). Role of induced and natural imbibition in frac fluid transport and fate in gas shales. *for the Hydraulic Fracturing Study: Fate and Transport*, *70*.

13. Cheng, Y. (2012). Impact of water dynamics in fractures on the performance of hydraulically fractured wells in gas-shale reservoirs. *Journal of Canadian Petroleum Technology*, *51*(02), 143-151.

14. Chenevert, M. E., & Pernot, V. (1998, January). Control of shale swelling pressures using inhibitive water-base muds. In *SPE Annual Technical Conference and Exhibition*. Society of Petroleum Engineers.

15. Cipolla, C. L., Lolon, E. P., Erdle, J. C., & Rubin, B. (2010). Reservoir modeling in shale-gas reservoirs. *SPE reservoir evaluation & engineering*, *13*(04), 638-653.

16. Civan, F. (2019). Effective Correlation of Stress and Thermal Effects on Porosity and Permeability of Naturally Fractured Formations by a Modified Power Law. *SPE Journal*, *24*(05), 2-378.

17. Dacy, J. M. (2010, January). Core tests for relative permeability of unconventional gas reservoirs. In *SPE Annual Technical Conference and Exhibition*. Society of Petroleum Engineers.

18. Darabi, H., Ettehad, A., Javadpour, F., & Sepehrnoori, K. (2012). Gas flow in ultra-tight shale strata. *Journal of Fluid Mechanics*, *710*, 641.
19. Darishchev, A., Lemouzy, P., & Rouvroy, P. (2013, January). On simulation of flow in tight and shale gas reservoirs. In *SPE Unconventional Gas Conference and Exhibition*. Society of Petroleum Engineers.
20. Dong, J. J., Hsu, J. Y., Wu, W. J., Shimamoto, T., Hung, J. H., Yeh, E. C., ... & Sone, H. (2010). Stress-dependence of the permeability and porosity of sandstone and shale from TCDP Hole-A. *International Journal of Rock Mechanics and Mining Sciences*, *47*(7), 1141-1157.
21. Dullien, F. A. (2012). *Porous media: fluid transport and pore structure*. Academic press.
22. Edwards, R. W., & Celia, M. A. (2018). Shale gas well, hydraulic fracturing, and formation data to support modeling of gas and water flow in shale formations. *Water Resources Research*, *54*(4), 3196-3206.
23. Elputranto, R., & Akkutlu, I. Y. (2020). Near-Fracture Capillary End Effect on Shale-Gas and Water Production. *SPE Journal*.
24. Eveline, V. F., Akkutlu, I. Y., & Moridis, G. J. (2017). Numerical simulation of hydraulic fracturing water effects on shale gas permeability alteration. *Transport in Porous Media*, *116*(2), 727-752.
25. Ewy, R. T. (2014). Shale swelling/shrinkage and water content change due to imposed suction and due to direct brine contact. *Acta Geotechnica*, *9*(5), 869-886.
26. Fakcharoenphol, P., Torcuk, M., Kazemi, H., & Wu, Y. S. (2016). Effect of shut-in time on gas flow rate in hydraulic fractured shale reservoirs. *Journal of Natural Gas Science and Engineering*, *32*, 109-121.
27. Fan, L., Thompson, J. W., & Robinson, J. R. (2010, January). Understanding gas production mechanism and effectiveness of well stimulation in the Haynesville Shale through reservoir simulation. In *Canadian unconventional resources and international petroleum conference*. Society of Petroleum Engineers.
28. Florence, F. A., Rushing, J., Newsham, K. E., & Blasingame, T. A. (2007, January). Improved permeability prediction relations for low permeability sands. In *Rocky mountain oil & gas technology symposium*. Society of Petroleum Engineers.
29. Ganjdanesh, R., Rezaveisi, M., Pope, G. A., & Sepehrnoori, K. (2016). Treatment of condensate and water blocks in hydraulic-fractured shale-gas/condensate reservoirs. *SPE Journal*, *21*(02), 665-674.
30. Geoquest, S. (1999). Eclipse 100 reference manual.
31. Ghanbari, E., & Dehghanpour, H. (2016). The fate of fracturing water: A field and simulation study. *Fuel*, *163*, 282-294.
32. Guo, X., Zou, G., Wang, Y., Wang, Y., & Gao, T. (2017). Investigation of the temperature effect on rock permeability sensitivity. *Journal of Petroleum Science and Engineering*, *156*, 616-622.
33. Gupta, R., & Maloney, D. R. (2016). Intercept method--A novel technique to correct steady-state relative permeability data for capillary end effects. *SPE Reservoir Evaluation & Engineering*, *19*(02), 316-330.
34. Holditch, S. A. (1979). Factors affecting water blocking and gas flow from hydraulically fractured gas wells. *Journal of Petroleum Technology*, *31*(12), 1-515.
35. Javadpour, F., Fisher, D., & Unsworth, M. (2007). Nanoscale gas flow in shale gas sediments. *Journal of Canadian Petroleum Technology*, *46*(10).

36. Jiang, J., & Yang, J. (2018). Coupled fluid flow and geomechanics modeling of stress-sensitive production behavior in fractured shale gas reservoirs. *International Journal of Rock Mechanics and Mining Sciences*, *101*, 1-12.

37. Jurus, W. J., Whitson, C. H., & Golan, M. (2013, September). Modeling water flow in hydraulically-fractured shale wells. In *SPE Annual Technical Conference and Exhibition*. Society of Petroleum Engineers.

38. Karniadakis, G. E., Beskok, A., & Gad-el-Hak, M. (2002). Micro flows: fundamentals and simulation. *Appl. Mech. Rev.*, *55*(4), B76-B76.

39. Klewiah, I., Berawala, D. S., Walker, H. C. A., Andersen, P. Ø., & Nadeau, P. H. (2020). Review of experimental sorption studies of CO2 and CH4 in shales. *Journal of Natural Gas Science and Engineering*, *73*, 103045.

40. Klinkenberg, L. J. (1941, January). The permeability of porous media to liquids and gases. In *Drilling and production practice*. American Petroleum Institute.

41. Knudsen, M. (1909). Die Gesetze der Molekularströmung und der inneren Reibungsströmung der Gase durch Röhren. *Annalen der Physik*, *333*(1), 75-130.

42. Lai, F., Li, Z., & Wang, Y. (2017). Impact of water blocking in fractures on the performance of hydraulically fractured horizontal wells in tight gas reservoir. *Journal of Petroleum Science and Engineering*, *156*, 134-141.

43. Lan, Q., Dehghanpour, H., Wood, J., & Sanei, H. (2015). Wettability of the Montney tight gas formation. *SPE Reservoir Evaluation & Engineering*, *18*(03), 417-431.

44. Langmuir, I. (1918). The adsorption of gases on plane surfaces of glass, mica and platinum. *Journal of the American Chemical society*, *40*(9), 1361-1403.

45. Leverett, M. (1941). Capillary behavior in porous solids. *Transactions of the AIME*, *142*(01), 152-169.

46. Li, C., Singh, H., & Cai, J. (2019). Spontaneous imbibition in shale: A review of recent advances. *Capillarity*, *2*(2), 17-32.

47. Liu, H. H., Ranjith, P. G., Georgi, D. T., & Lai, B. T. (2016). Some key technical issues in modelling of gas transport process in shales: a review. *Geomechanics and Geophysics for Geo-Energy and Geo-Resources*, *2*(4), 231-243.

48. Luo, P., Li, S., Knorr, K. D., & Nakutnyy, P. (2018, April). Underlying Mechanisms of Tight Reservoir Wettability and Its Alteration. In *SPE Improved Oil Recovery Conference*. Society of Petroleum Engineers.

49. Makhanov, K., Habibi, A., Dehghanpour, H., & Kuru, E. (2014). Liquid uptake of gas shales: A workflow to estimate water loss during shut-in periods after fracturing operations. *Journal of Unconventional Oil and Gas Resources*, *7*, 22-32.

50. Mason, G., & Morrow, N. R. (2013). Developments in spontaneous imbibition and possibilities for future work. *Journal of Petroleum Science and Engineering*, *110*, 268-293.

51. Mullen, J. (2010, January). Petrophysical characterization of the Eagle Ford Shale in south Texas. In *Canadian Unconventional Resources and International Petroleum Conference*. Society of Petroleum Engineers.

52. Naik, S., You, Z., & Bedrikovetsky, P. (2018). Productivity index enhancement by wettability alteration in two-phase compressible flows. *Journal of Natural Gas Science and Engineering*, *50*, 101-114.

53. Ostermeier, R. M. (2001). Compaction effects on porosity and permeability: Deepwater Gulf of Mexico turbidite. *Journal of Petroleum Technology*, *53*(02), 68-74.

54. Pang, Y., Soliman, M. Y., Deng, H., & Emadi, H. (2017). Analysis of effective porosity and effective permeability in shale-gas reservoirs with consideration of gas adsorption and stress effects. *Spe Journal*, *22*(06), 1-739.

55. Peng, D. Y., & Robinson, D. B. (1976). A new two-constant equation of state. *Industrial & Engineering Chemistry Fundamentals*, *15*(1), 59-64.

56. Rani, S., Padmanabhan, E., & Prusty, B. K. (2019). Review of gas adsorption in shales for enhanced methane recovery and CO_2 storage. *Journal of Petroleum Science and Engineering*, *175*, 634-643.

57. Rapoport, L. A., & Leas, W. J. (1953). Properties of linear waterfloods. *Journal of Petroleum Technology*, *5*(05), 139-148.

58. Richardson, J. G., Kerver, J. K., Hafford, J. A., & Osoba, J. S. (1952). Laboratory determination of relative permeability. *Journal of Petroleum Technology*, *4*(08), 187-196.

59. Rubin, C., Zamirian, M., Takbiri-Borujeni, A., & Gu, M. (2019). Investigation of gas slippage effect and matrix compaction effect on shale gas production evaluation and hydraulic fracturing design based on experiment and reservoir simulation. *Fuel*, *241*, 12-24.

60. Schmidt, K. A., Folas, G. K., & Kvamme, B. (2007). Calculation of the interfacial tension of the methane–water system with the linear gradient theory. *Fluid Phase Equilibria*, *261*(1-2), 230-237.

61. Singh, H. (2016). A critical review of water uptake by shales. *Journal of Natural Gas Science and Engineering*, *34*, 751-766.

62. Sondergeld, C. H., Ambrose, R. J., Rai, C. S., & Moncrieff, J. (2010, January). Micro-structural studies of gas shales. In *SPE Unconventional Gas Conference*. Society of Petroleum Engineers.

63. Sun, H., Chawathe, A., Hoteit, H., Shi, X., & Li, L. (2015). Understanding shale gas flow behavior using numerical simulation. *SPE Journal*, *20*(01), 142-154.

64. Virnovsky, G. A., Skjaeveland, S. M., Surdal, J., & Ingsoy, P. (1995, January). Steady-state relative permeability measurements corrected for capillary effects. In *SPE Annual Technical Conference and Exhibition*. Society of Petroleum Engineers.

65. Wang, L., Fu, Y., Li, J., Sima, L., Wu, Q., Jin, W., & Wang, T. (2017). Experimental study on the wettability of Longmaxi gas shale from Jiaoshiba gas field, Sichuan Basin, China. *Journal of Petroleum Science and Engineering*, *151*, 488-495.

66. Wyllie, M. R. J., & Gardner, G. H. F. (1958). The generalized Kozeny-Carman equation. Part 2. A novel approach to problems of fluid flow. *World Oil*, *146*(5), 210-228.

67. Xu, M., & Dehghanpour, H. (2014). Advances in understanding wettability of gas shales. *Energy & Fuels*, *28*(7), 4362-4375.

68. Yan, Q., Lemanski, C., Karpyn, Z. T., & Ayala, L. F. (2015). Experimental investigation of shale gas production impairment due to fracturing fluid migration during shut-in time. *Journal of Natural Gas Science and Engineering*, *24*, 99-105.

69. Yao, Y. M., Shi, A. F., Wang, X. H., & Liu, Z. F. (2019). A numerical well model considering capillary end effect for the low-permeability gas reservoir. *Oil & Gas Science and Technology–Revue d'IFP Energies nouvelles*, *74*, 87.

70. Yassin, M. R., Dehghanpour, H., Wood, J., & Lan, Q. (2016). A theory for relative permeability of unconventional rocks with dual-wettability pore network. *SPE Journal*, *21*(06), 1-970.

71. Yu, W., & Sepehrnoori, K. (2014). Simulation of gas desorption and geomechanics effects for unconventional gas reservoirs. *Fuel*, *116*, 455-464.

72. Yuan, W., Li, X., Pan, Z., Connell, L. D., Li, S., & He, J. (2014). Experimental investigation of interactions between water and a lower Silurian Chinese shale. *Energy & Fuels*, *28*(8), 4925-4933.
73. Zhang, T., Li, X., Li, J., Feng, D., Li, P., Zhang, Z., ... & Wang, S. (2017). Numerical investigation of the well shut-in and fracture uncertainty on fluid-loss and production performance in gas-shale reservoirs. *Journal of Natural Gas Science and Engineering*, *46*, 421-435.
74. Zhou, Z., Wei, S., Lu, R., & Li, X. (2020). Numerical Study on the Effects of Imbibition on Gas Production and Shut-In Time Optimization in Woodford Shale Formation. *Energies*, *13*(12), 3222.

5. Appendix A: Numerical discretization and convergence

The primary variables are gas pressure and gas saturation, labeled p and s in the following. Let index i denote grid point number where $i = 1$ is at the outlet boundary $X = 0$ and $i = 2, 3, ...$ denotes points separated by intervals $\Delta X_{i+\frac{1}{2}} = X_{i+1} - X_i$ which may not be equal. The number of points depends on the case studied.

Assume the saturation s_i and pressure p_i are known at point i with location X_i. Equations (27) and (28) are discretised on the left hand side and solved for pressure and saturations in point $i + 1$ as follows:

$$
(30) \quad p_{i+1} = p_i + [d_X p]\left(p_{i+\frac{1}{2}}, s_{i+\frac{1}{2}}\right)\Delta X_{i+\frac{1}{2}}, \qquad s_{i+1} = s_i + [d_X s]\left(p_{i+\frac{1}{2}}, s_{i+\frac{1}{2}}\right)\Delta X_{i+\frac{1}{2}},
$$
$$
(i = 1, ..., N_x - 1).
$$

The functions $[d_X p]$ and $[d_X s]$ refer to the expressions on the right hand side in (27) and (28) being evaluated at the pressure and saturation averaged between point i and $i + 1$:

$$
(31) \quad p_{i+\frac{1}{2}} = 0.5(p_i + p_{i+1}), \qquad s_{i+\frac{1}{2}} = 0.5(s_i + s_{i+1}).
$$

The parameters $p_{i+\frac{1}{2}}$ and $s_{i+\frac{1}{2}}$ are first assumed equal to p_i and s_i, respectively, in (30) to give first estimates of p_{i+1} and s_{i+1}. The distance to point $i + 1$, namely $\Delta X_{i+\frac{1}{2}}$ is then selected such that:

$$
(32) \quad s_{i+1} = s_i + \Delta s^{ref}
$$

where Δs^{ref} is a set saturation increment. Then $p_{i+\frac{1}{2}}$ and $s_{i+\frac{1}{2}}$ are reevaluated until they no longer change. For sharp saturation gradients the distance is selected according to fixed saturation intervals Δs^{ref}, while when the saturation gradient is low (outside the end effect region) fixed spatial intervals ΔX^{ref} are applied. Once the total length reaches $X = 1$ the algorithm stops.

$$
(33) \quad \Delta X_{i+\frac{1}{2}} = \min\left[\frac{\Delta s^{ref}}{[d_X s]\left(p_{i+\frac{1}{2}}, s_{i+\frac{1}{2}}\right)}, \Delta X^{ref}\right],
$$

The algorithm is initiated by using the boundary conditions (22) to fix the values in the first cell:

$$
(34) \quad p_1 = p_{fr}, \qquad s_1 = s_g^{eq}
$$

6. Appendix B: Numerical validation against commercial simulator

The presented steady state model is validated by comparison against a dynamic simulation generated by the commercial software ECLIPSE 100 (Geoquest 1999) taking into account some key elements of the model such as: gas displacing water at inlet pressure p_{in}, production at zero capillary pressure and a given fracture pressure p_{fr}, given capillary pressure and relative permeability curves and gas compressibility. Slip and rock compressibility were not considered. Reference parameters were used. The water saturation profile at steady state (when water is no more produced) is shown in **Figure 12** comparing results from Eclipse (red circles) and our model (implemented in MATLAB, full line). Both models capture that gas does not displace all the mobile water, that nonresidual water is found at the inlet, and that there is a sharp saturation gradient close to the outlet where the highest saturations towards $s_w = 0.89$ do not cover any significant interval.
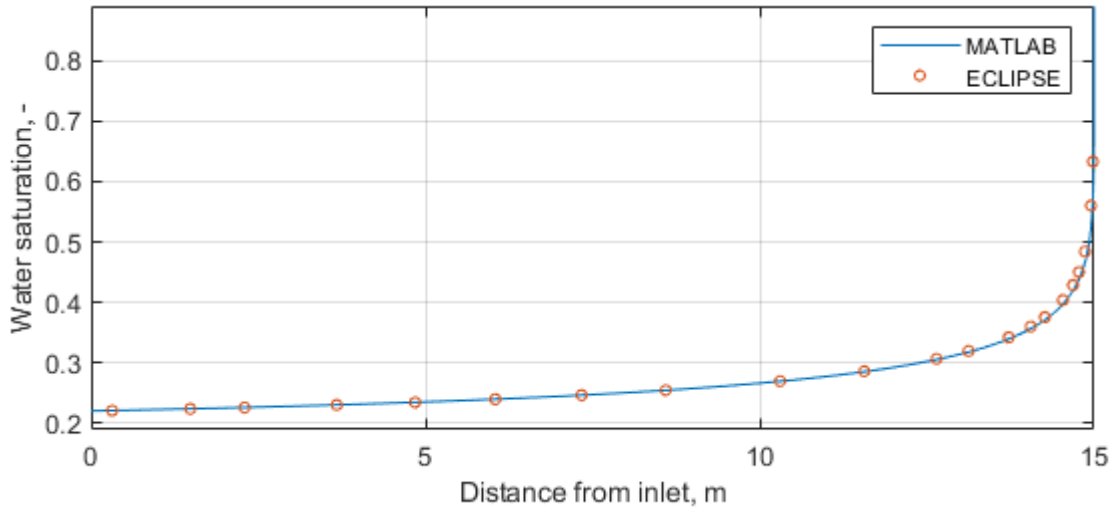
Figure 12 Comparison of Eclipse simulation and the model presented in this work under same conditions.

7. List of tables

Table 1 Input parameters used as base case in the simulations taken from 1: Yu et al. (2014), 2: Edwards and Celia (2018), 3: Evans and Civan (1994), 4: Schmidt et al. (2007), 5: Dacy (2010) and 6: Byrnes (2011). $\Delta s\_g^{\wedge}eq$ denotes $s\_g^{\wedge}eq-s\_gr$.

Table 2 Compressibility parameters for different cases. The low, medium and high values are reported in Dong et al. (2010) for Chinsui shale. The LO c_K also corresponds to Marcellus shale from Rubin et al. (2019).

Table 3 Calculated gas mass fluxes for the reference case where gas compressibility and slip assumptions are modified.

Table 4 Calculated gas mass fluxes and how much they are lowered by blockage for different gas Corey exponents in the reference case.

Table 5 Calculated gas mass fluxes with and without blockage and their ratio for different shale compressibilities in the reference case.

Table 6 Calculated gas mass fluxes with and without blockage and their ratio for different saturation tortuosities in the reference case assuming the HI compressibility case.

8. List of figures

Figure 1 Geometry of the system. Gas is flowing through the system according to a fixed pressure drop, entering from the right boundary x=L while water is trapped by capillary forces. The saturation at the outlet x=0 is fixed by the zero capillary pressure.

Figure 2 Gas density vs pressure at T_res.

Figure 3 Porosity (a) and permeability (b) vs pressure for different compressibility cases (INC, LO, MED, HI) with parameters from Table 2. Full and dashed lines in (b) indicate intrinsic and apparent permeability, respectively.

Figure 4 Gas relative permeability (a) for different Corey exponents n_g (5 is the reference). Also (b) scaled and unscaled water-gas capillary pressure based on a rescaled mercury drainage curve from Byrnes (2011) to residual water and gas saturations from Dacy (2010). The cross over saturation has been varied using different Δs_g^{eq} (values indicated) where 0.001 corresponds to the experimental data.

Figure 5 Normalized gas saturation (a,b), normalized pressure (c,d) and apparent permeability (e,f) spatial distributions for different relative drawdowns ($\Delta P/(\Delta P\_ref)$), varied using p_fr. Other parameters are kept at reference values. Water blockage is accounted for in the left figures but not in the right.

Figure 6 Normalized gas saturation (a,b), normalized pressure (c,d) and apparent permeability (e,f) spatial distributions where gas is either compressible ('Com') or not ('Inc') and slip is accounted for ('slip') or not for the reference case. Water blockage is accounted for in the left figures but not in the right.

Figure 7 Spatial distributions of normalized gas saturation (a) and normalized pressure (b) for different wetting states, according to the indicated value of $\Delta s\_g^{eq}=s\_g^{eq}-s\_gr$ (low values means more water-wet). The corresponding case with no water blockage (NBL) is indicated with dashed line.

Figure 8 Mass flux m_g vs drawdown ($\Delta P = P\_in - P\_fr$) (a) for the case with no water blockage (NBL) and blockage cases with different wetting indicated by $\Delta s\_g^{eq} = s\_g^{eq} - s\_gr$ (lower value means more water-wet). Relative fluxes on log scale for the same cases (how high flux is obtained without blockage compared to with blockage) are plotted in (b) against relative drawdown ($\Delta P / \Delta P\_ref$).

Figure 9 Spatial distributions of normalized gas saturation (a) and normalized pressure (b) for different gas Corey exponents (values indicated) for the reference case. The corresponding case with no water blockage (NBL) is indicated with dashed line.

Figure 10 Normalized gas saturation (a,b), normalized pressure (c,d) and apparent permeability (e,f) spatial distributions for different compressibility cases (INC, LO, MED, HI). Water blockage is accounted for in the left figures but not in the right.

Figure 11 Normalized gas saturation (a), normalized pressure (b), apparent permeability (c) and gas Corey exponent (d) spatial distributions for different values of Δn_g considering the HI compressibility case. The coresponding case without water blockage (NBL) is shown in dashed line.

Figure 12 Comparison of Eclipse simulation and the model presented in this work under same conditions.